

Comparison of wave impact tests at large and full scale: results from the Sloskel project

W. Lafeber⁽¹⁾, L. Brosset⁽²⁾, H. Bogaert⁽¹⁾

¹MARIN, Hydro Structural Services, Wageningen, The Netherlands

²GTT (Gaztransport & Technigaz), Saint-Rémy-lès-Chevreuse, France

ABSTRACT

Wave impact tests were conducted at two different scales within the Sloskel Joint Industry Project. In 2009 unidirectional breaking waves were generated in a flume at scale 1:6. The waves impacted on an instrumented wall. These tests were repeated at scale 1:1 in 2010. The piston motions were scaled by maintaining the Froude number. At both scales, the tests were performed with water and air at atmospheric pressure and ambient temperature. The compressibility of the liquid and the gas, and other properties such as the surface tension of the liquid were therefore equal at both scales.

The measured impact pressures at scale 1:6 and 1:1 are compared deterministically in this paper to define by how much the Froude-scaling of the impact pressures is biased by the fact that the properties of the liquid and the gas are not scaled.

This deterministic comparison requires that the global flow at scale 1:1 starting from the wave piston to the instant just before the first contact with the wall is Froude-similar to the flow at scale 1:6. Only then the differences between the measured pressures at the two scales can entirely be attributed to the fact that the properties of the liquid and the gas were not scaled. Froude-similar global flows were obtained for these tests by carefully controlling the piston motion and the water depth at both scales and by minimising the effect of the wind at full scale.

The comparison of the impact pressures for the Froude-similar global flows shows that the loading processes 'building jets along the wall from the impact area' and 'compression of entrapped air' are not Froude-similar when the compressibility of the gas is not scaled. The one-dimensional model of Bagnold (1939) is used to correct the loading process 'compression of entrapped air' measured at scale 1:6, resulting in a similar load to the one measured at scale 1:1.

KEY WORDS: Sloshing, LNG carrier, Containment System, scaling, model test, Froude, impact pressure, Elementary Loading Processes, flume tank, breaking wave

INTRODUCTION

Sloshing model tests are the basis of any sloshing assessment for a new membrane LNG carrier project (Gervaise et al. (2009)). These sloshing model tests are performed at GTT with model tanks at scale 1:40 ($\lambda=40$), installed on the platform of a six-degree-of-freedom hexapod. The excitation motions are scaled from calculated ship motions at full scale by maintaining the Froude number. This means that the time is

scaled by $1/\sqrt{\lambda}$ as the length is scaled by $1/\lambda$ and the gravitational acceleration is maintained. The tanks are filled with water and a mixture of nitrogen and sulphur hexafluoride such that the ratio between the density of the gas and the liquid is equal at model and full scale. The tank walls are flat and rigid. Up to 300 pressure sensors are used to capture the sloshing pressures in the impact areas. Long duration tests are required in order to obtain converged statistical pressures.

The statistical pressure results have to be scaled to full scale in order to derive design loads. The approach for scaling is not obvious as multi-physics occur within the impacts. An important step forward has recently been made: through several investigations the physics involved in these impacts could be linked to loading processes.

First of all it is useful to consider the flow inside a partially filled tank in two parts: the global flow and the local flow in the vicinity of and during the impacts.

Global flow

The global flow involves the propagation of the surface waves in the tank which defines the initial conditions of the local flow. The division between the global and the local flow is based on the reasonable assumption that the local flow does not affect the global flow statistically. Repeating the same excitations several times leads to impacts at the same time instants and locations, even for long duration tests.

The wave propagation is governed by the balance between the inertial and gravitational forces, i.e. the Froude number. Since the excitations of the hexapod are set by maintaining the full scale Froude number, sloshing model tests generate a statistical sample of initial conditions for the local flow that is representative of the full scale conditions.

Local flow

In contrast to the rather deterministic behaviour of the global flow, the local flow and corresponding impact pressure appear to be randomly distributed. Only statistical post-processing of long duration tests enables getting repeatable sloshing loads.

The loading processes involved in the local flow are unravelled in Lafeber et al. (2012). Three Elementary Loading Processes (ELP) have been identified as the building blocks of any load possibly induced by a wave impact. This means that any part of a pressure or a force signal recorded on a structure is a result of one or a combination of these three ELPs. They are: the direct impact (ELP1), the building jet along the structure (ELP2), and the compression of entrapped or escaping gas

(ELP3). Each ELP is directly related to one of the main physical phenomena involved during impact, respectively, liquid compressibility, liquid change of momentum and gas compressibility.

Typical combinations of the ELPs have been identified for wave impacts on a flat wall and a wall covered with bulges. The most typical combination begins with ELP ‘compression of escaping gas’ that occurs as the gas tries to escape while the wave approaches the structure. Then, ELP ‘direct impact’ takes place. Finally ELP ‘building jet’ occurs as building jets are induced by the direct impact. This ELP interacts with ELP ‘compression of pulsating gas’ after entrapment is achieved due to the direct impacts. This combination is schematically represented in Figure 1. This combination of ELPs can take place under the following circumstances, i.e. when a gas-pocket wave impact occurs onto a flat wall, or a wall covered with bulges, when a wave trough reattaches to the wall after separation over a bulge during the run-up process and when a jet induced by a first impact hits a bulge.

The corresponding physical phenomena, i.e. liquid compressibility, liquid change of momentum and gas compressibility are added to Figure 1. The other physical phenomena involved during a liquid impact interfere with the ELPs. They might influence the intensity of each ELP and the interaction between them, but are not sources of new kinds of ELPs. This has led to the conclusion that the list of ELPs is complete. These phenomena interfere in the following way.

The phase of gas-escaping in between the wave and the structure can be split in two stages. At first the gas escapes almost freely and the gas flow can be considered as incompressible. A transfer of momentum between the liquid and the gas intervenes which is ruled by the density ratio between gas and liquid. The flow of escaping gas will accelerate further and create instabilities at the free surface, known as the Kelvin-Helmholtz instabilities. These instabilities are considered to be the main cause of variability for the local flow and the corresponding impact pressures.

At a certain moment, the escaping gas will start to compress, because it cannot escape quickly enough to keep the same density in the volume remaining in between the wave and the structure. Moreover, if the gas is the vapour of the liquid in thermodynamic conditions close to the equilibrium, phase transition will interfere with the compression of escaping gas and with the compression of entrapped gas. The elasticity of the impacted structure (hydro-elasticity) interferes with each ELP. Finally, the Rayleigh-Taylor instability of the free surface may develop during the compression of an entrapped gas pocket. This phenomenon contributes to the damping of the pressure oscillations.

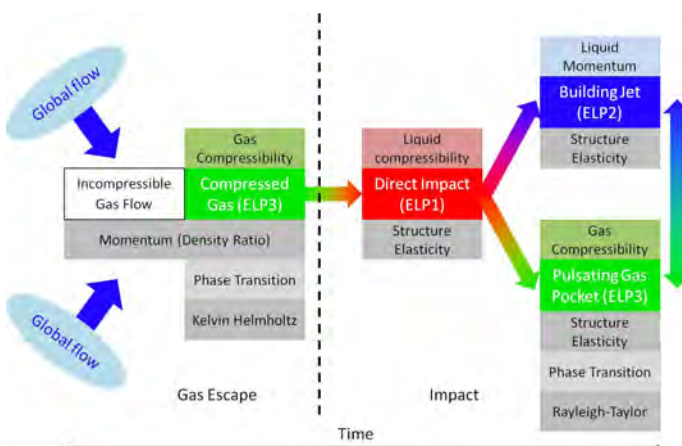


Figure 1. Schematic representation of the most typical combination of ELPs in relation to their main and associated phenomena.

Complete and Partial Froude-scaling

As has been mentioned, similarity of the initial conditions of the local flow, i.e. the velocities of the liquid and the gas at the end of the global flow phase, is achieved by maintaining the Froude number for the excitations of the hexapod. This means that the pressure inside the liquid and the gas at the end of the global flow phase follows a Froude-scaling, i.e. the amplitude is scaled by $1/\lambda$ and the time by $1/\sqrt{\lambda}$. Braeunig et al. (2009) showed that the pressure inside the local flow up to the impact pressures will also follow the Froude-scaling if all liquid and gas properties involved during the local flow are adjusted to the conditions imposed by the Froude-scaling, i.e. their length is scaled by $1/\lambda$ and their time is scaled by $1/\sqrt{\lambda}$. For example, the speed of sound of the gas and the liquid should be scaled by $1/\sqrt{\lambda}$. Under these conditions the sloshing model tests would follow a Complete Froude Scaling (CFS).

These conditions are however not fulfilled during sloshing model tests because:

1. Gas compressibility, liquid compressibility, liquid momentum, transfer of momentum between liquid and gas, Kelvin-Helmholtz and Rayleigh-Taylor instabilities are taken into account at model scale but are not all adjusted to the conditions imposed by the Froude-scaling.
2. Phase transition and the elasticity of the structure are not taken into account at model scale.
3. Bulges of the membrane, i.e. corrugations of MarkIII or raised edges of NO96, are not taken into account at model scale.

The local flow at model scale thus biases a Froude-scaling of the impact pressures. This situation is referred to as Partial Froude Scaling (PFS). The question is how much the Froude-scaling of the impact pressures is biased.

The effect of the elasticity of the structure on the PFS is described in Brosset et al., (2011). It was concluded that this effect is not significant for the tested wave impact intensities. A small change in the intensity of the ELPs and the interaction between them was observed.

The effect of the bulges is described in Lafeber et al. (2012). New local flow situations intervene as the wave interacts with the bulges. They are mainly the reattachment of the flow after separation over a bulge during the run-up process and the impact on a bulge by a building jet running along the wall. These biases are caused by a lack of geometric similarity at the same scale. A geometric similarity at two different scales would however not help if the objective is to compare model tests to full scale. It would not only be difficult to capture these additional local flow situations during sloshing model tests with tank walls covered with bulges, but these flow situations would physically not be the same as at full scale, because the corresponding properties of the liquid are not scaled. For example, the building jet impacting a bulge would have a thickness of less than 1 mm at scale 1:40. Such a jet would be largely affected by the un-scaled viscosity and surface tension of the liquid.

The effect of the transfer of momentum between the gas and the liquid is defined by Maillard and Brosset (2009). This transfer of momentum is governed by the density ratio. A heavier gas escapes with more difficulty between the wave and the structure. As a consequence, the higher the density ratio, the higher the rate of gas entrapment. A bias in the density ratio will thus change the combination of the ELPs. The study showed that there is a significant bias when sloshing model tests are carried out with a density of 0.0012 (air and water) instead of 0.004 (NG and LNG). GTT therefore adopted a solution where sloshing model tests are carried out with water and a mixture of nitrogen and

sulphur hexafluoride such that the ratio between the density of the gas and the liquid is equal at model and full scale.

The effect of the gas compressibility, the liquid compressibility, the liquid momentum, the Kelvin-Helmholtz and the Rayleigh-Taylor instabilities on the PFS is studied in this paper by comparing wave impact tests carried out at two different scales. These tests were performed within the Sloshel project. The Froude number and the density ratio were maintained.

Deterministic comparison of wave impact tests at different scales

Bogaert et al. (2010) have tried to compare deterministically the full scale wave impact tests on the NO96 containment system carried out within the Sloshel project at the end of 2007, and the large scale wave impacts tests on a flat wall carried out within the same project in 2009. It was however concluded that a deterministic comparison was not possible as there was a lack of repeatability of the global flow at full scale and a lack of similarity between the global flow at full and large scale. The high frequency content in the steering signal spectrum was difficult to follow mechanically at full scale, leading to a lack of repeatability and similarity. The repeatability of the global flow at full scale, being tested in an outdoor flume, was further spoiled by the prevailing wind.

These aspects were improved during the full scale wave impact tests on the MarkIII containment system performed in April 2010 in the framework of the Sloshel project. In this paper, these full scale tests are compared to the large scale tests performed on the corrugated wall in 2009. The test set-ups are first presented in the next section. After that, it is explained how Froude similar global flows are generated. Finally, the comparison of the local flow at both scales is presented.

TEST SET-UPS AT LARGE AND FULL SCALE

The large scale (1:6) tests were carried out in the Schelde flume, an indoor facility. The full scale tests were performed in the Delta flume, an outdoor facility where the full scale NO96 tests were also performed in 2007. During the full scale MarkIII tests, tents were installed to cover a large part of the flume. Both flumes are operated by Deltares. Breaking waves are generated by piston-type second-order wave steering systems, installed at one end of the flume. Transverse test walls were placed at the other flume ends. Both walls shown in Figure 2 were designed and instrumented by MARIN. A detailed description of the test set-ups is given in Kaminski et al. (2010).

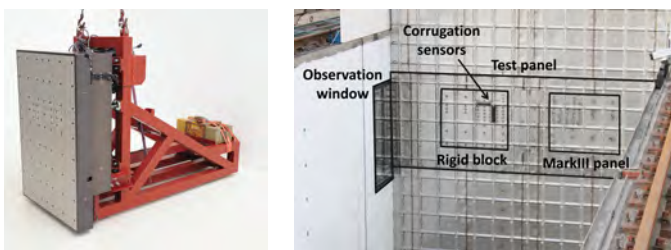


Figure 2. Tests walls at large scale (left) and full scale (right).

The large scale test wall was a 1:6 copy of the full scale test wall used during the NO96 tests, however, designed with an exchangeable wall cover. A flat cover and a cover with the MarkIII corrugations at scale 1:6 were used. The geometric similarity between the large scale tests with the corrugated cover and the full scale MarkIII tests was not complete. First, the length scale for the distance between the piston and the wall was 6.14. At full scale the wall was placed at 145.16 m from the piston such that appropriate connection points on the floor could be made for the concrete wall. This location was set in 2007 for the NO96 test. The wall at large scale could not be placed at 24.19 m

(145.16 m/6) as the steel window frames of the tank walls would have blocked the view of the flow in front of the wall. The wall was therefore moved forward such that the wall surface was aligned with the window frame, as shown in Figure 3, giving a distance between the piston and the wall of 23.63 m. The resulting length scale of 6.14 has been used for the wave generation.



Figure 3. Location of high speed cameras at large (left) and full (right) scales

Secondly, the same pressure sensors were used at both scales. The diameter of the sensitive membrane was 1.3 mm. Furthermore, the pressure sensors were not placed at exactly similar locations. The wall at large scale was equipped with two rigid blocks. Twelve pressure sensors were installed on each block at scaled vertical positions with respect to the NO96 tests. The positions are given in Figure 4. The row of pressure sensors was located at the height where the maximum pressures were expected. To better capture the impact pressures the number of pressure sensors were increased for the full scale MarkIII tests. The rigid block and the MarkIII panel contained both 52 pressure sensors. Their positions on the rigid block are also given in Figure 4.

Finally, the corrugations were not placed at similar locations. At large scale the corrugation grid was placed around the pressure sensor configuration for NO96 tests. Three lines of horizontal corrugations could be placed on the boxes such that a maximum number of pressure sensors was not covered and one line was located just above the row of pressure sensors. These positions could not be maintained at full scale because the upper line of horizontal corrugations, where the maximum loads were expected, would have been too close to the edge of the MarkIII panel. This would not have been representative for the loads on the MarkIII cargo containment system. The corrugations were therefore moved downward as shown in Figure 4.

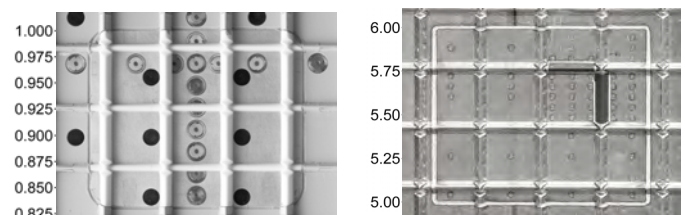


Figure 4. Position of pressure sensors and corrugations at large (left) and full (right) scales. Positions are given in meters.

At both scales the motion of the piston and the wave elevation were measured. Several wave gauges were placed in the flumes at similar locations, using the length scale of 6.14. The closest wave gauges to the wall, i.e. respectively 4.49 m and 27.59 m from the test wall, are used in this study. These measurements were recorded at 200 Hz at large scale and 50 Hz at full scale, and were synchronised with the data acquisition system of the pressure sensors, sampling at 50 kHz. The synchronisation uncertainty was in the order of 5 ms at large scale and 20 ms at full scale.

High speed cameras were used at both scales to capture the shape of the waves just before and during the impacts on the wall. These cameras were synchronised with the data acquisition system of the pressure sensors. At large scale, several cameras captured the wave through the transparent wall of the flume. One camera, see Figure 3, shot video at 5 kHz, giving a synchronisation uncertainty with the pressure measurements of 0.2 ms. At full scale, an observation window with a height of 1.5 m and a width of 0.9 m was installed in the west side of the flume, see Figure 2. Behind this window a pit was created, see Figure 4, to place three cameras, providing a full window view, a half window view and a close-up around a corrugation. These cameras were respectively shooting video at 5 kHz, 5 kHz and 1.2 kHz, giving a synchronisation uncertainty with the pressure measurements of 0.2 ms and 0.8 ms.

GENERATION OF FROUDE-SIMILAR GLOBAL FLOWS

At both scales, the tests were performed with water and air at atmospheric pressure and ambient temperature. The waves were generated using a focusing method. The piston generated successive waves of increasing length and height. The wave train was created in such a way that all waves add at one longitudinal position of the flume, the focal point, and produced a single, large breaking wave.

The full scale NO96 tests used a set of parameters for the steering signal that were tuned to obtain a horizontal velocity of the breaking wave crest as close as possible to 10 m/s. This set is referred to as wave type A. It appeared that the high frequency content in the corresponding steering signal spectra was difficult to follow mechanically by the piston at full scale. During tests at both scales with wave type A, it appeared moreover that a small leading wave always broke just in front of the focused wave, resulting in a perturbed flow. Since both aspects led to a lack of repeatability and similarity, a new set of parameters was established during the large scale tests. This set is referred to as wave type B. Several test series using wave type B were performed during the large scale tests and the full scale Mark III tests.

Global flow at large scale

At large scale, tests with wave type B resulted in repeatable global flows that corresponded to each steering signal. The piston at large scale was able to mechanically follow the steering signal with a good accuracy. This is illustrated in Figure 5 where a steering signal is shown together with six corresponding motions of the piston.

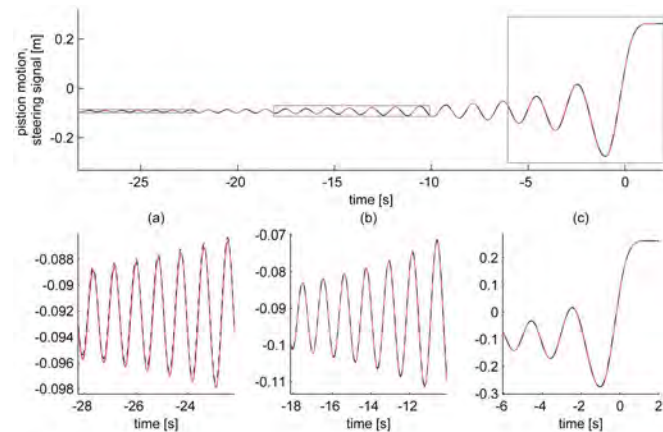


Figure 5. A steering signal of wave type B (dashed black line) and six corresponding motions of the piston at large scale (red line: tests L66, L68, L69, L70, L71 and L119).

Five tests (L66, L68, L69, L70 and L71) were carried out with the flat wall cover, one (L119) with the corrugated wall cover. The measurements are aligned with the last stroke of the piston. The time is set to $t=0$ when the last stroke passes $x=0$. The test with the maximum difference between the steering signal and the piston motion within this set is determined. The absolute difference between both signals is defined in order to catch both the phase and the amplitude differences. The area under this difference line, divided by the integration time is used to quantify the accuracy of the piston motions. The result, called the score, is therefore the difference between the actual distance covered by the piston and the expected one over the chosen duration. The score is 0.7 mm for an integration time going from -28.24 s to 2.01 s. This value is likely smaller than the accuracy of the measurement of the piston motion.

The resulting waves were still very close after travelling over the major part of the flume, as indicated in Figure 6 by the measured wave elevations at 4.49 m from the test wall. The measurements are aligned with the last stroke of the piston. The maximum difference between the wave elevations resulted in a score of 1.5 mm for an integration time going from -3.63 s to 6.85 s. As Kimmoun et al. (2010) demonstrated how much the water depth could affect the global flow, these repetitions were achieved with careful checks of the water depth.

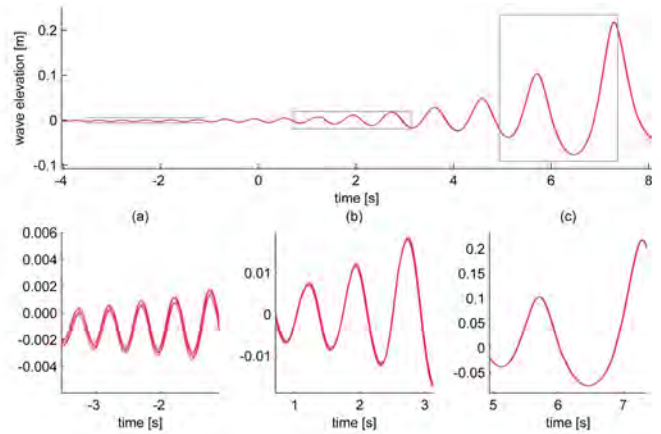


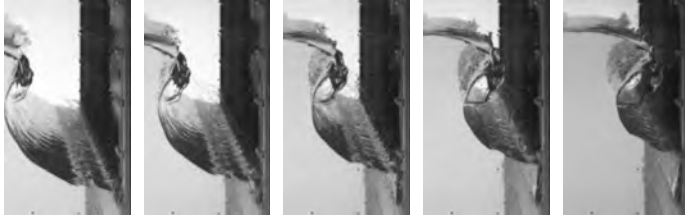
Figure 6. Wave elevations at 4.49 m from the test wall at large scale for the six repetitions of the piston motions given in Figure 5 (tests L66, L68, L69, L70, L71 and L119)

Good repeatability is maintained during the last stages of the wave propagation, as illustrated in Figure 7. The observations of the wave shape in front of the wall are presented for the test with the corrugated wall cover (L119) and for one of the tests with the flat wall cover (L66). The wave broke before the wall generating an air-pocket type of impact (see e.g. Bogaert (2010), Brosset (2009)). A large liquid string developed from the crest at the side walls of the flume. As a consequence the wave shape was not perfectly two-dimensional.

The pictures from the high speed camera recordings in Figure 7 were not aligned with the wave elevation measurements as the wave shape changes too much within the synchronisation uncertainty of 5 ms. The video recordings were therefore synchronized with the pressures on the wall. The time instant where the pressure on the wall exceeds a threshold value of 0.024 bar ($= 0.15 \text{ bar}/6.14$) is used as reference. The last observations are 6.1 ms ($= 15 \text{ ms}/\sqrt{6.14}$) before this time instant.



(a) Large scale test L66 on flat wall cover



(b) Large scale test L119 on corrugated wall cover

Figure 7. Wave shape in front of the test wall at large scale for tests presented in Figure 5 and Figure 6. Time step is 6.1ms ($15\text{ms}/\sqrt{6.14}$).

Global flow at full scale

At full scale, the steering signals for wave type B were scaled from the steering signals at large scale by maintaining the Froude number. This should have resulted in Froude-similar global flows. It appeared however, that the piston at full scale was not able to accurately follow the steering signal. Figure 8 presents the difference between a steering signal and the corresponding motion of the piston. It is apparent that the amplitude and the phase differ for both the high and the low frequency components, resulting in a score of 31 mm for an integration time going from -70 s to 5 s.

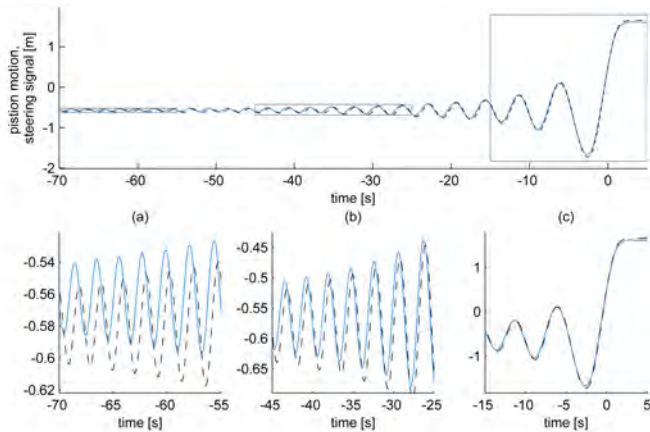


Figure 8. Steering signal of wave type B (dashed black line) and corresponding motion of the piston at full scale (blue line).

Following the approach presented in Kimmoun et al. (2010), a relation was defined in the frequency domain between the steering signals and the motions of the piston. Both the differences in the amplitude and the phase were considered. This transfer function was then used to define a steering signal for which the real motion of the piston at full scale equals the Froude scaled motion of the piston at large scale.

The result is illustrated in Figure 9 for the large scale test with the corrugated wall cover (L119) presented in Figure 5. The motions of the piston at full scale are shown for five tests (M51, M52, M53, M54 and M55) along with their target value from large scale. The maximum difference between the piston motions at large (after Froude scaling) and full scale (after the correction) is determined and resulted in a score of 9 mm for an integration time going from -70 s to 5 s. The score

quantifies the accuracy of the piston, including the transfer function correction. The transfer function has thus improved the accuracy of the piston with a factor of approximately 3. The full scale accuracy is still lower than the scaled accuracy at large scale ($0.7\text{ mm} \cdot 6.14 = 4.3\text{ mm}$), causing necessarily a difference between the global flows at both scales.

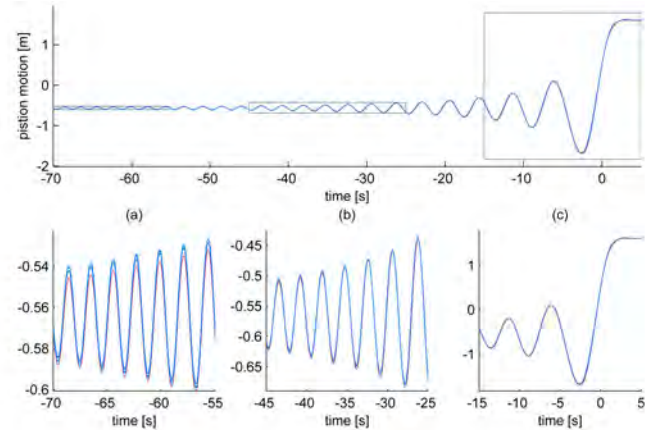


Figure 9. Froude scaled motions of the piston at large scale for the test with corrugated wall cover (red line: L119) presented in Figure 5 and five corresponding motions of the piston at full scale (blue line: M51, M52, M53, M54 and M55).

However, for the majority of the tests at full scale, the main difference with the large scale tests was caused by an uncertainty on the water depth and by the effect of the wind on the propagation of the waves. As has been mentioned before, it is important to carefully control the water depth because an uncertainty of a few millimetres in the water depth leads to an uncertainty of centimetres on the focal point and therefore reduces the repeatability of the global flow. The ability to accurately measure the water depth was also affected by the wind conditions at full scale. Although the flume was covered with tents over a large part, the free-surface still moved a little prior to testing on a windy day. This increased the uncertainty to measure and thus to master the water depth conditions. Furthermore, the wind had an effect on the propagation of the waves through the flume. This effect further reduced the repeatability of the global flow because the wind conditions changed during the three-week-long test campaign.

The variation of the global flow at full scale is illustrated in Figure 10. The measured wave elevations at 27.59 m from the test wall are presented for the five tests (M51, M52, M53, M54 and M55), for which the piston motions are shown in Figure 9.

The difference in wave elevation between test M51, M52, and M53 is small, namely a score of 6 mm for an integration time going from -9 s to 17 s. These tests were carried out successively on the same day. The difference between test M54 and M55, both performed the next day, is also small with a score of 2 mm. The difference between these two and the three previous tests is however considerable which could be explained by different prevailing wind conditions during the two testing days. The latter score of 17 mm is approximately 2 times larger than the scaled score from large scale ($1.5\text{ mm} \cdot 6.14 = 9.2\text{ mm}$).

Figure 11 shows the wave shapes of tests M51 and M52 (first day) and Figure 12 those of tests M54 and M55 (day after). The types of resulting impacting waves are different. In case of test M51 and M52, an air-pocket type of impact was generated. In case of test M54, the crest and the trough converged to a small area at the wall generating a flip-through type of impact (see e.g. Bogaert (2010), Brosset (2009)).

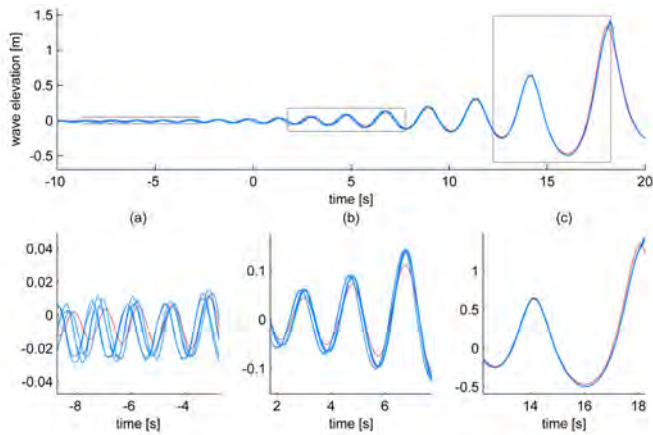


Figure 10. Wave elevations at 27.59 m from the test wall for the piston motions given in Figure 9. Five tests (blue line: M51, M52, M53, M54 and M55) are shown at full scale along with their target value at large scale (red line).

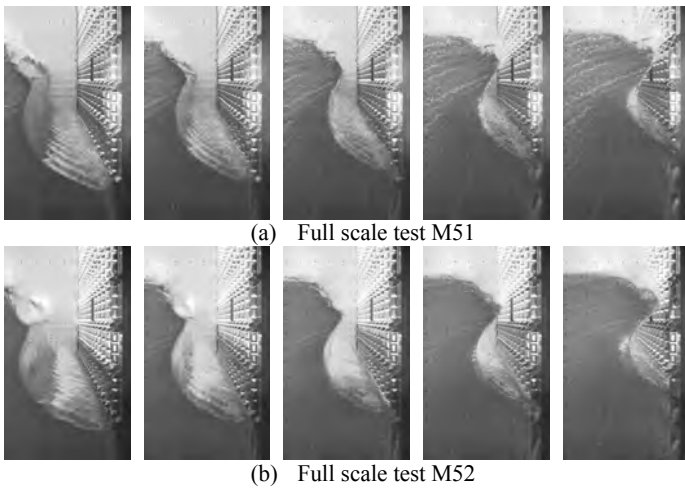


Figure 11. Wave shape in front of the test wall at full scale for full scale tests M51 (top) and M52 (bottom) presented in Figure 9. Time step is 15 ms.

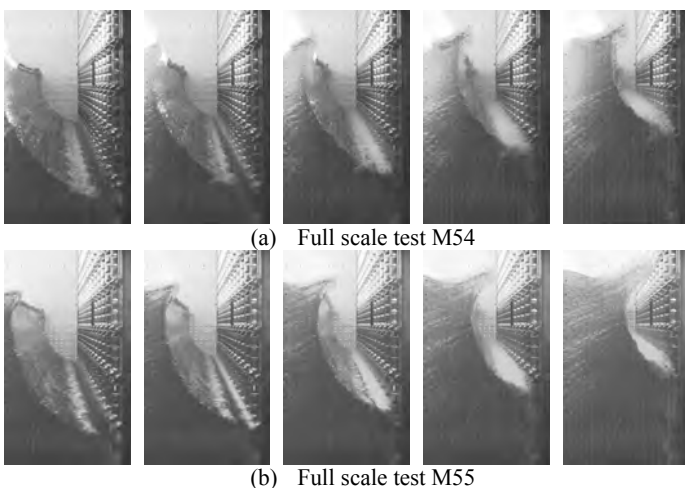


Figure 12. Wave shape in front of the test wall at full scale for full scale tests M54 (top) and M55 (bottom) presented in Figure 9. Time step is 15 ms.

The full scale observations in Figure 11 (M51, M52) and Figure 12 (M54, M55) can be directly compared with the observations in Figure 7 at large scale (L66, L119) as all parameters have been relevantly scaled. The observation area follows the length scale of 6.14. The time step is scaled by maintaining the Froude number. The observations are aligned with the pressures on the wall. The time instant where the pressure on the wall exceeds a threshold value of 0.15 bar is used as reference. The last observations are at 15 ms before this time instant.

Figure 7, Figure 11 and Figure 12 show that M51 and M52 match rather well with L66 and L119, and M54 and M55 do not match.

Froude-similar global flows

The reduced repeatability at full scale complicated the generation of the required Froude-similar global flows at both scales. A large number of tests have been carried out at full scale to eventually achieve this goal. The following procedure has been applied to select the appropriate full scale tests from the database.

The difference between the wave elevations at full scale and the Froude-scaled target values at large scale was defined for each test and the corresponding scores were determined. After that, the wave shapes in front of the wall were compared in order to define which value of the score was acceptable. Values up to approximately 13 mm for an integration time going from -9 s to 17 s, appeared to be acceptable for the difference in wave elevations at 27.59 m before the test wall. Two groups of full scale tests proved to be appropriate.

The first group corresponds to the large scale tests L119, presented in Figure 7b. Thirty tests were carried out at full scale based on the initial L119 piston motion. The five full scale tests given in Figure 9 were selected as giving the maximum accuracy for the piston motions. The scores for the difference between the wave elevations at large and full scale at similar locations corresponding to 27.59 m from the wall at full scale, are shown in Table 1.

Table 1. Scored difference between wave elevations of tests at full scale at 27.59 m from the wall and Froude scaled wave elevations of large scale test L119 at the corresponding location.

Test	M51	M52	M53	M54	M55
Difference (mm)	11	11	11	16	16

M51, M52 and M53, performed on the same day, have a comparable score of around 11 mm. M54 and M55 performed the day after have a worse score of 16 mm. The comparison between Figure 7 (b) and Figure 12 clearly indicates that a score of 16 mm is not acceptable. The comparison between Figure 7 (b) and Figure 11 indicates that a score up to 11 mm might be acceptable. The wave contours obtained from these recordings, presented in Figure 13 (a), show that the global flows were indeed very similar. Test M51, M52 and M53 have therefore global flows that match the best the Froude-similarity with the global flow of L119. There is however a small difference in the shape of the crest and in the amount of air that is being entrapped. A slightly smaller pocket was formed at full scale.

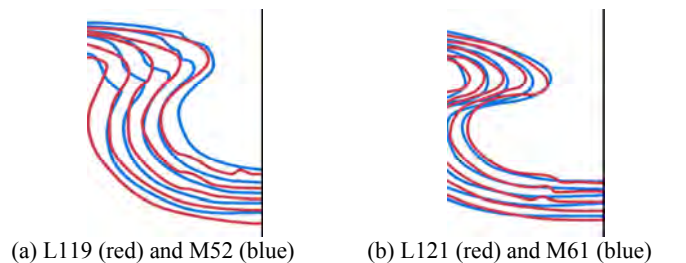


Figure 13. Comparison of wave contours at large (red) and full (blue) scale. Contours are obtained from the high speed recordings.

The second group corresponds to the large scale test L121. The wave shape in front of the test wall is shown in Figure 14. An air-pocket type of impact was generated. A large liquid string developed from the crest at the side walls of the flume, making the wave shape not perfectly two-dimensional.



Figure 14. Wave shape in front of the test wall for large scale test L121 with corrugated wall cover. Time step is 6.1 ms ($15 \text{ ms}/\sqrt{6.14}$).

Nineteen full scale tests were carried out based on the L121 piston motion. Fourteen were selected as giving the maximum accuracy for the piston motions. The first five minimum scores for the difference between the wave elevations at large and full scale are shown in Table 2. There is a gradual increase of the scores.

Table 2. Scored difference between wave elevations of tests at full scale at 27.59 m from the wall and Froude scaled wave elevations of large scale test L121 at corresponding point.

Test	M61	M62	M60	M59	M69
Difference (mm)	12	13	13	14	15

Figure 15 shows the wave shapes of tests M61 and M62 and Figure 16 those of tests M59 and M69. The types of resulting impacting waves were similar. Air-pocket type of impacts were generated. For the higher scores (M59, M69), the waves broke later resulting in a steeper lower part of the air pocket. For all tests, a large liquid string developed from the crest at the side walls of the flume, making the wave shape not perfectly two-dimensional.

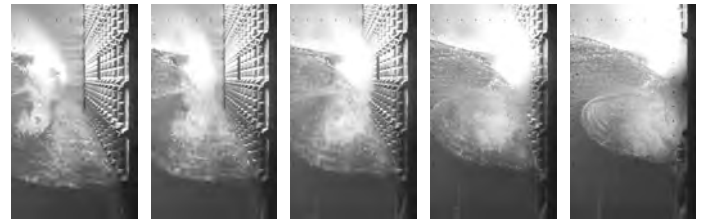
The full scale observations in Figure 15 (M61, M62) and Figure 16 (M59, M69) can be directly compared with the observations in Figure 14 at large scale (L121) as all parameters have been relevantly scaled. The observation area follows the length scale of 6.14. The time step is scaled by maintaining the Froude number. The observations are aligned with the pressures on the wall. The time instant where the pressure on the wall exceeds a threshold value of 0.15 bar at full scale is used as a reference. The last observations are at 15 ms before this time instant.

The comparison between M59, M69 (Figure 16) and L121 (Figure 14) shows that the differences become too large for a score above 14mm. The waves in M59, M69 broke too late resulting in a steeper lower part of the air pocket. The comparison between M61, M62 (Figure 15) and L121 is better. The wave contours obtained from these recordings, presented in Figure 13 (b), show that the global flows were indeed similar. Tests M60, M61 and M62 have therefore global flows that match the best the Froude-similarity with the global flow of L121.

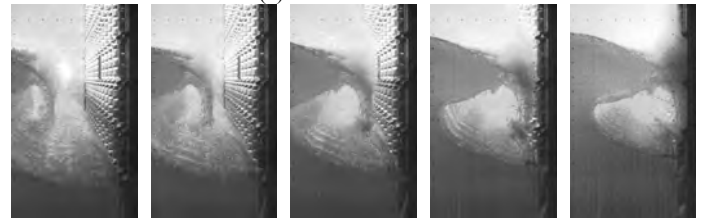
The Froude-similarity is better in case of M60, M61 and M62 than in case of M51, M52 and M53, although the scores were slightly higher. This indicates that the difference at 27.59 m from the wall at full scale can be used to sort out the main differences, but that the final assessment has to be made based on the comparison of the wave shapes in front of the wall.

COMPARISON OF LOCAL FLOWS

The selected tests were performed at both scales with water and air at atmospheric pressure and ambient temperature. As a consequence, the speed of sound in the liquid and in the gas, and the surface tension of the liquid were equal at both scales. The liquid and the gas compressi-



(a) Full scale test M61



(b) Full scale test M62

Figure 15. Wave shape in front of the test wall at full scale for test M61 (top) and M62 (bottom). Time step is 15 ms.



(a) Full scale test M59



(b) Full scale test M69

Figure 16. Wave shape in front of the test wall at full scale for test M59 (top) and M69 (bottom). Time step is 15 ms.

bilities, and the Kelvin-Helmholtz and the Rayleigh-Taylor instabilities were therefore not adjusted to the conditions imposed by a Froude-scaling. Moreover, the geometric similarity was not complete as the corrugations were positioned at different locations at both scales. The selected tests were thus performed under the conditions of a Partial Froude Scaling. The local flows of the selected tests were therefore supposed to bias the Froude-similarity that was initiated by the global flows.

The local flows of the selected tests at both scales are shown in Figure 17 and Figure 20. Test M52 is considered together with L119, and M62 together with L121 despite the fact that M52 and M62 have the second best scores for the global flow similarity. Both tests turned out to have the clearest high speed camera and pressure recordings. Test M51, M53, M61 and M60 will be used further on in the paper when the pressures in the air pockets are studied in more detail.

The full scale observations in Figure 17 (M52) and in Figure 20, (M62) can be directly compared with the large scale observations in Figure 17 (L119) and in Figure 20 (L121) as all parameters have been relevantly scaled. The observation area follows the length scale of 6.14. The time step is scaled by maintaining the Froude number. The observations are aligned with the pressures on the wall. Time instant t_1 is the instant

when the pressure on the wall exceeds a threshold value of 0.15 bar at full scale and 0.024 bar at large scale ($=0.15 \text{ bar}/6.14$).

The pressure measurements are given in Figure 18, Figure 19, Figure 21 and Figure 22. Dynamic pressures are presented. The pressures at large scale have been Froude-scaled and their positions are scaled by the length scale 6.14. A time span of 250 ms is considered in the left columns. The right columns show the first 40 ms. t_1 corresponds to $t=0$ s. The number of pressure sensors and their location were not equal at both scales. There were five sensors placed at full scale in between two horizontal corrugations compared to two at large scale. Therefore, the different ELPs could be better captured at full scale. Differences in the pressure measurements at both scales are therefore not only a result of differences in the local flows.

The observations in Figure 17 and Figure 20 are the continuation of those given for the global flow (respectively Figure 7 (b) compared to Figure 11 (b) and Figure 14 compared to Figure 15 (b)). The last observations given for the global flows are at 15 ms before t_1 .

The transition between the global and the local flow starts at the moment when the transfer of momentum between the liquid and the gas starts to affect the flow. This time instant cannot easily be identified, especially when the density ratio between the liquid and the gas is equal at both scales. The transfer of momentum between the liquid and the gas would be different at both scales if the density ratios were different. The time instant when the contours of the resulting wave shapes in front of the wall are no longer similar, can then be used to mark the start of the local flow.

For all the selected tests, the wave broke before the wall. The overturning crest impacted the wall, entrapping an air pocket. This flow situation concurs with the most typical combination of ELPs, schematically represented in Figure 1. The approach of the crest forces the air to escape in between the crest and the wall. The escaping air creates a spray around the tip of the crest i.e. the Kelvin-Helmholtz instabilities, and will compress (ELP3) at the moment it cannot escape quickly enough. When the crest makes contact with the wall, ELP 'direct impact' (ELP1) takes place. Building jets along the wall (ELP2) are induced by this direct impact and an air pocket is entrapped. The air pocket is compressed (ELP3) by the forward moving wave front and the run-up of the trough.

Large scale test L119

For the large scale test L119, the crest impact took place just above the horizontal corrugation at 5.71 m, whereby the lower part of the crest touched the corrugation. Spray in the form of thin liquid films can be seen around the tip of the crest before impact, in the last observation of Figure 7 (b) and the first of Figure 17 (a).

ELP1 was not captured by the pressure sensors. The first contact occurred under sensor PL3 in between t_1 and t_2 . At t_1 the crest did not yet touch the wall but the compression of the escaping air (ELP3) already started, resulting in a pressure rise that was captured by PL5 to PL8. At t_2 the air pocket was closed and was nearly at its maximum compression (ELP3). Sensor PL5 to PL8 were located in the air pocket.

The direct impact induced a vertical jet that ran upward along the wall, propagating toward the horizontal corrugation at 6.06 m. The building jet (ELP2) passed successively PL3 and PL2, resulting in a sudden increase of the pressure. These sensors also captured the remote influence of the entrapped air pocket, once they were located in the crest. The intensity of this influence depends on the distance to the air pocket as the pressure within the crest ensures a continuity between the air pocket pressure and the ullage pressure. Later on, these sensors also captured the compression of the entrapped air directly, once they entered in the upward moving air pocket.

The air pocket oscillated with a frequency of 21.3 Hz. The pocket compression was maximal just after t_2 , resulting in a pressure of 2.5 bar. An expansion phase started afterwards. The maximum volume was reached around t_4 , with a corresponding pressure of 0.9 bar below the atmospheric pressure. Meanwhile, Rayleigh-Taylor instabilities were formed on the air pocket surface that can clearly be seen in Figure 17(a) (large bubbles behind the pocket). After one oscillation, the pressure was damped by approximately 63 %.

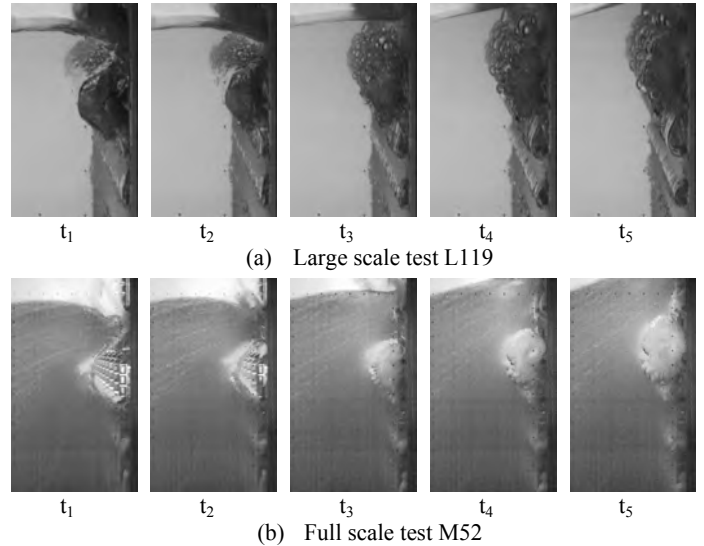


Figure 17. Local flows for the Froude-similar global flows obtained with large scale test L119 (top) and full scale test M52 (bottom). Time step is 10 ms.

Full scale test M52

For the full scale test M52, the crest impact took place at similar height as for test L119, however, this time just under a horizontal corrugation. This was caused by the fact that the corrugations were located differently. This horizontal corrugation is located at 5.78 m. A spray of water drops was present around the tip of the crest before impact, as can be seen in Figure 11 (b) and Figure 17 (b).

The first contact (ELP1) occurred just above PM2 in between t_1 and t_2 . At t_1 the crest did not yet touch the wall but the escaping air (ELP3) was already compressed. This was captured by PM2 to PM7. At t_2 the air pocket was closed and compressed (ELP3). Sensor PM2 to PM7 were located in the air pocket.

The direct impact induced two vertical jets (ELP2). One ran upward over the horizontal corrugation. The other jet moved downward, successively passing PM2, PM3 and PM4, resulting in a sudden increase of the pressure that was added to the pressure induced by the compression of the entrapped air. Once located in the crest, these sensors also captured the remote influence of the air pocket. The air pocket oscillated with a frequency of 8.6 Hz. The compression of the pocket was maximal just before t_3 , resulting in a pressure of 1.9 bar. An expansion phase started afterwards. The maximum volume of the pocket was reached at $t=79$ ms, giving a pressure of 0.3 bar below the atmospheric pressure. Meanwhile, Rayleigh-Taylor instabilities were formed on the air pocket surface that can clearly be seen in Figure 17 (b). After one oscillation, the pressure was damped by approximately 83 %.

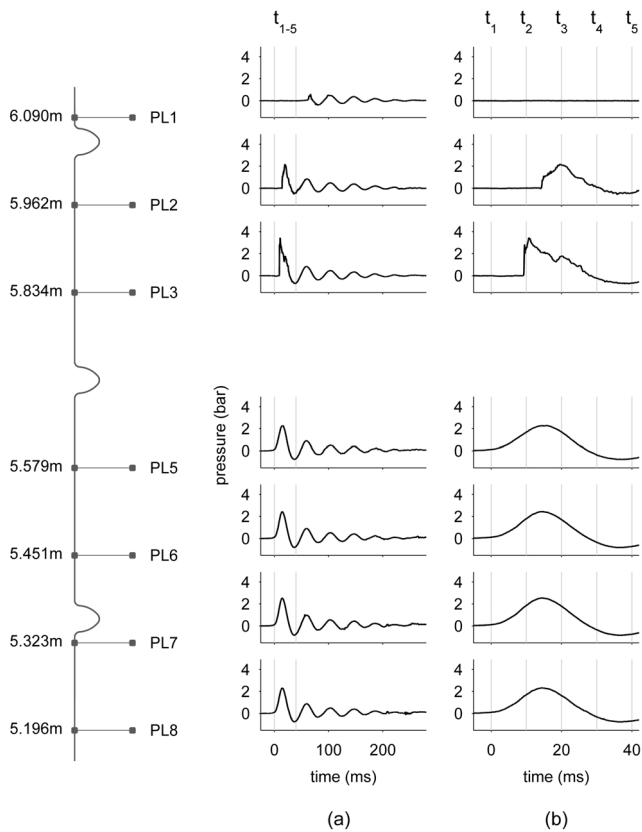


Figure 18. Pressure time traces for large scale test L119. Values have been Froude-scaled.

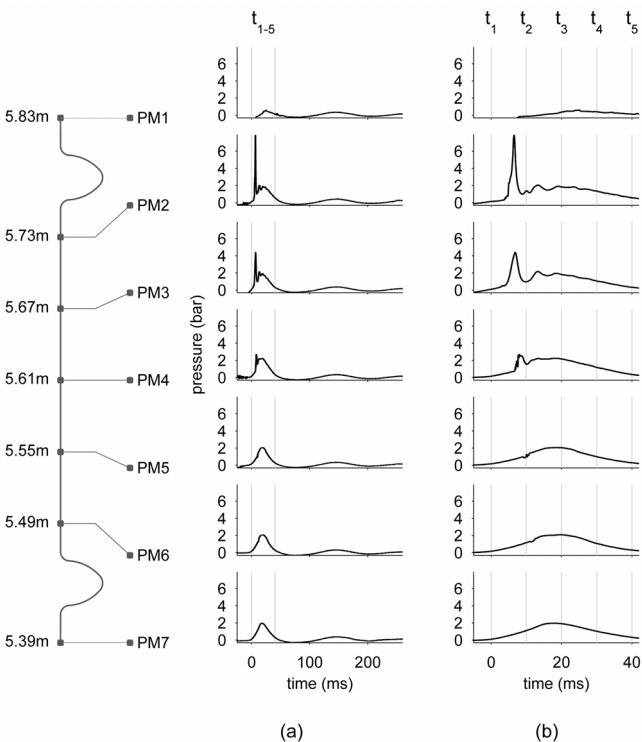


Figure 19. Pressure time traces for full scale test M52

Large scale test L121

For the large scale test L121, the crest impact took place in between the horizontal corrugations at 5.36m and 5.71m, closer to the lower one. Spray in the form of thin liquid films is clearly present around the tip of the crest as can be seen in Figure 14 and Figure 20 (a). The first contact occurred in the vicinity of PL6 at 5.45 m. ELP1 is likely captured by PL6 just after t_1 . At t_1 the crest did not yet touch the wall but the escaping air (ELP3) was already compressed, as captured by PL7 and PL8. When the direct impact occurred, sensors PL7 and PL8 were located in the air pocket. The direct impact induced a vertical jet (ELP2) that ran upward along the wall, passing by sensor PL5. The building jet impacted the horizontal corrugation at 5.71 m, separated from the wall and reattached further upwards. A new building jet was then formed that passed by PL3 and PL2. Neither the impact on the horizontal corrugation at 5.71 m nor the reattachment was captured by the sensors.

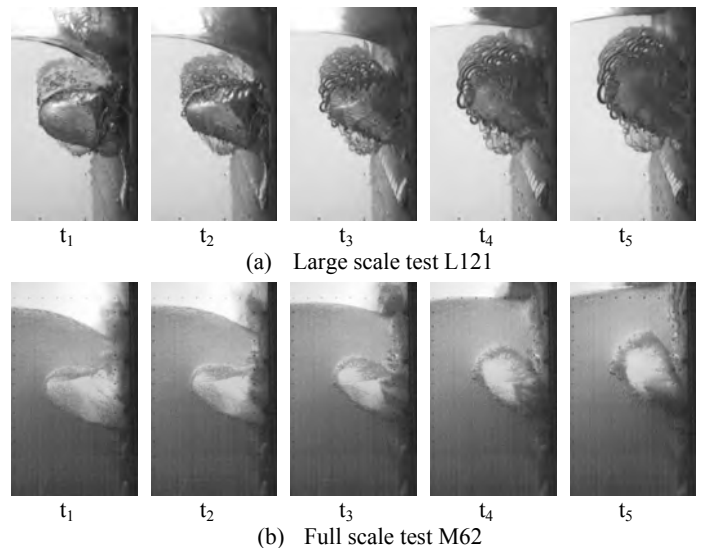


Figure 20. Local flows for the Froude-similar global flows obtained with large scale test L121 (top) and full scale test M62 (bottom). Time step is 10 ms.

Sensors PL1 to PL6 also captured the remote influence of the air pocket, once located in the crest. Later on, they captured the compression of the entrapped air directly, once they entered the upward moving air pocket. The air pocket oscillated with a frequency of 18.2 Hz. The compression of the pocket was maximal just after t_3 , resulting in a pressure of 1.6 bar. An expansion phase started afterwards. The pocket reached its maximum volume at $t=40$ ms, giving a pressure of 0.6 bar below the atmospheric pressure. Meanwhile, Rayleigh-Taylor instabilities were formed on the air pocket surface (see the bubbles behind the pocket in Figure 20 (a)). After one oscillation, the pressure was damped by approximately 45 %.

Full scale test M62

For the full scale test M62, the crest impact took place at a similar height as for test L121, however, just above a horizontal corrugation, caused by the fact that the corrugations were located differently. A spray of water was present around the tip of the crest as can be seen in Figure 15 (b) and Figure 20 (b). ELP1 was not captured by the pressure sensors. The first contact occurred in between PM5 and PM6 just before t_2 . At t_1 the crest did not yet touch the wall but the escaping air (ELP3) was already compressed. This was captured by the sensors above and below the oncoming contact point (PM2 to PM7). The

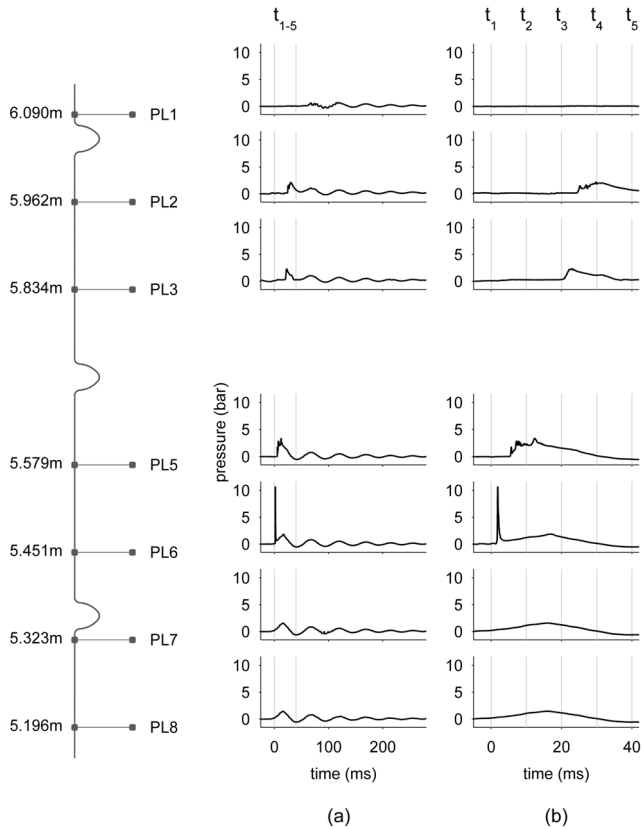


Figure 21. Pressure time traces for large scale test L121. Values have been Froude-scaled.

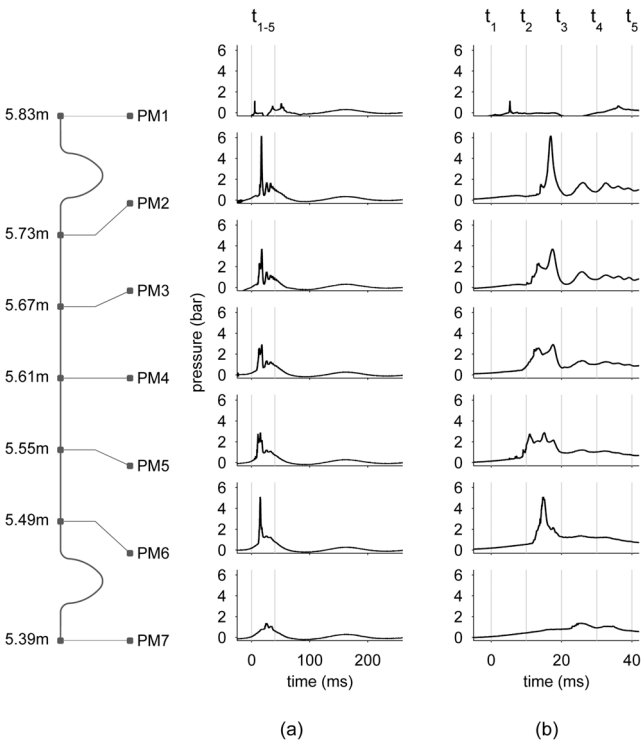


Figure 22. Pressure time traces for full scale test M62

pocket was closed at t_2 and compressed (ELP3). Sensor PM7 was located in the pocket. The direct impact induced two vertical jets (ELP2). One that ran upward, successively passing PM5 to PM2 resulting in a sudden increase of the pressure. This building jet impacted the horizontal corrugation at 5.78 m. This impact caused a pressure wave downwards, increasing the pressure at PM2, PM3 and PM4 for a second time. At PM5 the pressure wave nearly vanished. A small increase, the third one, can be observed just before t_3 . The other building jet moved downward, passing PM6. The building jet impacted the horizontal corrugation at 5.44 m. This caused a pressure wave upwards, increasing the pressure at PM6 and PM5 for the second time. The first and second increase at PM6 followed each other quickly. There is a change in the slope at approximately two bar, that marks very likely the transition. The second rise at PM5 is in between ELP2 and the increase due to the pressure wave coming downward from the corrugation at 5.78m.

Sensors PM1 to PM6 also captured the remote influence of the air pocket below, once located in the crest. The air pocket oscillated with a frequency of 7.8 Hz. The compression of the pocket was maximal around t_4 , resulting in a pressure of 0.9 bar. The expansion of the pocket started afterwards. The pocket reached its maximum volume at $t=96$ ms, giving a pressure of 0.1 bar below the atmospheric pressure. Meanwhile, Rayleigh-Taylor instabilities were formed on the air pocket surface (see Figure 20 (b)). After one oscillation, the pressure was damped by approximately 70 %.

Biases induced by Partial Froude Scaled local flows

The above descriptions show that the measured pressures at large scale do not match the measured pressures at full scale when they are Froude-scaled. The local flows, which followed the conditions of Partial Froude Scaling, biased the Froude-similarity that was initiated by the global flows. Four differences between the local flows at both scales are present.

1. Spray around the tip of the crest

The sprays induced by the tangential flow of gas around the tip of the crest were not similar: Thin liquid films were formed at large scale, whereas clouds of water drops were formed at full scale. The balance between the inertial forces and the surface tension forces was not equal at both scales because the surface tension of the liquid was not scaled. The surface tension forces were therefore relatively higher at large scale, resulting in Kelvin-Helmholtz instabilities with more coherent water films.

2. Interaction between the local flow and the corrugations

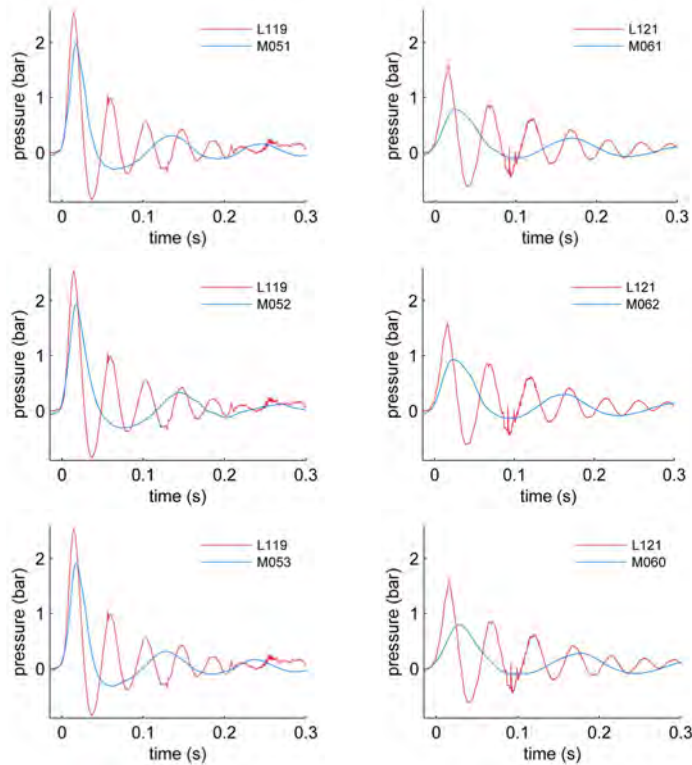
The local flow interacted differently with the corrugations at both scales because the corrugations were located differently. As a result, the intensity of the ELPs was different, in particular ELP1 (the pressure wave induced by the impact of a building jet on a corrugation, and the reattachment of the flow) and ELP2. It was therefore not possible to quantify the effect of the other biases on ELP1 and ELP2. This would actually hardly be possible in any case because ELP1 and ELP2 are sensitive to the Kelvin-Helmholtz instabilities which make them largely variable at each scale. A large number of tests would be required in order to obtain converged statistical pressures. Furthermore the number of pressure sensors to capture them was smaller at large scale.

3. Compression of entrapped air (ELP3)

The entrapped air was compressed differently at both scales. The pressures in the air pockets of tests L119, M52, L121 and M63 are shown in detail in Figure 23. The pressures at large scale have been Froude-scaled. The pressures in the air pockets of the other Froude-similar global flows M51, M53, M61 and M60 are also given. L119 is compared to M51, M52 and M53 in Figure 23 (a). L121 is compared to

M61, M62 and M60 in Figure 23 (b).

The global flows of the large scale test L121 and the full scale tests M61, M62 and M60 were very Froude-similar, as has been shown in Figure 13 (b). The differences between the pressures in the air pocket at both scales can therefore be attributed entirely to a bias of the local flow. In the case of M51, M52 and M53, the global flows were slightly less Froude-similar to the large scale test L119. A smaller air pocket was entrapped at full scale (Figure 13 (a)). The difference in the air pocket pressure observed in Figure 23, can therefore not be attributed entirely to a bias in the local flow. If the global flows had been even more Froude-similar, a larger air pocket would have been entrapped at full scale and the pressure in the air pocket would have been smaller at full scale.



(a) Large scale test L119 and full scale tests M51, M52 and M53

(b) Large scale test L121 and full scale tests M61, M62 and M60

Figure 23. Pressures in the air pockets at large (red) and full (blue) scale. Pressures at large scale have been Froude-scaled.

The characteristics of the pressures in the air pocket are summarised in Table 3 for L119, M51, M52 and M53, and in Table 4 for L121, M61, M62 and M60. The pressure amplitude is characterized by the maximum (p_{max}) and the minimum (p_{min}) of the time trace. The time history is characterized by the rise time (t_r) and the natural period (T). The rise time was defined by two times the difference between the time instants at which the pressure is respectively 50% and 100% of p_{max} . In addition, the damping ratio (ζ) was defined based on the assumption that the pressure decays according to $\exp(-\zeta t/T)$.

The Froude-scaled maxima from large scale were larger by up to a factor of two. In the case of L119, the difference would have been larger if the global flows at full scale had been more Froude-similar. Furthermore, the Froude-scaled rise times were shorter by up to a factor of two, and the frequencies were higher by up to a factor of 2.5. Finally, the damping ratios at large scale were smaller by up to a factor of two.

These differences have little effect on the maximum local pressure, because the compression of the entrapped air contributed little to the local pressure. The local pressure (p_{max}) was approximately 2 bar. However, the observed differences have a significant effect on the maximum global force. The compression of the entrapped air contributed significantly to the global force because its loaded area including its remote influence was larger than the size of the MarkIII panel, resulting in forces of approximately 200 kN on an area 1.2 m².

Table 3. Characteristics of pressures in the air pockets for large scale test L119 and full scale tests M51, M52 and M53. Pressure at large scale has been Froude-scaled, denoted by L119_{Fr}.

	L119 _{Fr}	M51	L119 _{Fr} / M51	M52	L119 _{Fr} / M52	M53	L119 _{Fr} / M53
p_{max} (bar)	2.5	2.0 (1.29)		1.9 (1.31)		1.9 (1.32)	
p_{min} (bar)	0.9	0.3 (2.80)		0.3 (2.79)		0.3 (2.71)	
p_{max}/p_{min} (-)	3.0	6.4 (0.46)		6.3 (0.47)		6.1 (0.49)	
t_r (ms)	13	16 (0.79)		18 (0.71)		16 (0.79)	
$1/T$ (Hz)	21.3	9.7 (2.20)		8.6 (2.46)		10.2 (2.08)	
T/t_r (-)	3.7	6.3 (0.58)		6.4 (0.57)		6.0 (0.61)	
ζ (-)	0.14	0.28 (0.50)		0.27 (0.53)		0.28 (0.51)	

Table 4. Characteristics of pressures in the air pockets for large scale test L121 and full scale tests M61, M62 and M60. Pressure at large scale has been Froude-scaled, denoted by L121_{Fr}.

	L121 _{Fr}	M61	L121 _{Fr} / M61	M62	L121 _{Fr} / M62	M60	L121 _{Fr} / M60
p_{max} (bar)	1.6	0.8 (2.03)		0.9 (1.71)		0.8 (1.99)	
p_{min} (bar)	0.6	0.1 (6.16)		0.1 (4.88)		0.1 (6.18)	
p_{max}/p_{min} (-)	2.6	7.8 (0.33)		7.3 (0.35)		8.0 (0.32)	
t_r (ms)	18	34 (0.52)		30 (0.58)		36 (0.48)	
$1/T$ (Hz)	18.2	7.5 (2.43)		7.8 (2.32)		7.2 (2.51)	
T/t_r (-)	3.1	3.9 (0.80)		4.2 (0.74)		3.8 (0.82)	
ζ (-)	0.10	0.17 (0.59)		0.18 (0.56)		0.16 (0.61)	

The air pocket is compressed mainly by the forward movement of the wave front and the run-up of the trough. It acts like a mass-spring system. The pushing liquid (the mass) interacts with the restoring gas (the spring). The balance between the pushing liquid and the restoring gas was not equal at both scales. The mass and its initial velocity were Froude-similar because the global flows were Froude-similar. The spring stiffness however, was not Froude-similar, because the compressibility was not scaled. The spring was therefore relatively too stiff at large scale, resulting in relatively higher frequencies at large scale. Moreover, as the frequency is higher the mass needs to decelerate and accelerate in a shorter period of time, requiring larger forces. The pressures were therefore relatively too large at large scale.

Moreover, the restoring gas acts like a nonlinear spring. The time trace is sinusoidal when the spring is compressed minimally. The time trace is characterized by a sharp crest and a flat trough when the spring is compressed significantly. The actual compression is smaller at large than at full scale, for example a p_{max} of 0.4 bar is measured at large scale and 1.4 bar at full scale. The time traces at full scale therefore have sharper crests and flatter troughs. As a consequence, the ratios p_{max}/p_{min} and T/t_r are larger at full scale by up to a factor of 3 and 1.5 respectively.

During the oscillation of the air pocket, the pushing mass of water flows around the pocket. The kinetic energy of this pushing liquid decreases, resulting in a damping of the pressure oscillations. At the start of the compression the kinetic energy was Froude-similar. As a result of a relatively too stiff spring, the pressures at large scale were

too large at their first maximum. They were approximately identical to the pressures at full scale at the second maximum of the full scale pressures, indicating that the kinetic energy of the liquid at this time instant was relatively lower at large scale. The loss of kinetic energy was thus larger at large scale. The relatively too stiff spring mitigated the impacts more at large scale than would be expected by a Froude-scaling. The damping ratio, indicating the reduction in pressure between two successive maxima, was lower at large scale, because the frequency was relatively higher.

Moreover, the damping was affected by the Rayleigh-Taylor instabilities. These instabilities are formed at the interface between two fluids of different densities when the lighter fluid accelerates to the heavier fluid. The instabilities were formed at the air pocket surface whenever the air accelerated to the water, gradually breaking-up the air pocket and thus damping the pressures. The air starts to accelerate towards the water before the end of each compression. The Rayleigh-Taylor instabilities occurred at a higher ratio at large scale because the frequency of oscillation was relatively higher. As a result, the damping due to the Rayleigh-Taylor instabilities had to be larger at large scale. On the other hand, the surface tension forces were relatively larger at large scale, making it harder to break-up the air pocket, as explained by Hinze (1955). As a result, although the Rayleigh-Taylor instabilities occurred at a lower rate at full scale, they might have had a larger effect on the damping than at large scale. It cannot be concluded from the tests which of the two was dominant.

Bogaert et al. (2010) studied the compression of entrapped gas further by considering the one-dimensional Bagnold piston model (see Bagnold (1939) and Mitsuyasu (1966)). The main parameters of this model are given in Figure 24. The liquid of density ρ_l and length L compresses a gas pocket against a rigid wall. Initially the gas pocket has a length x_0 and a pressure p_0 . The initial velocity of the piston is U_0 . The ullage pressure on the other side of the piston keeps the constant value p_0 .

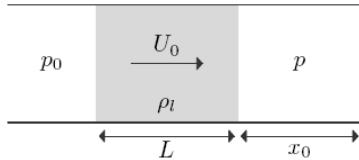


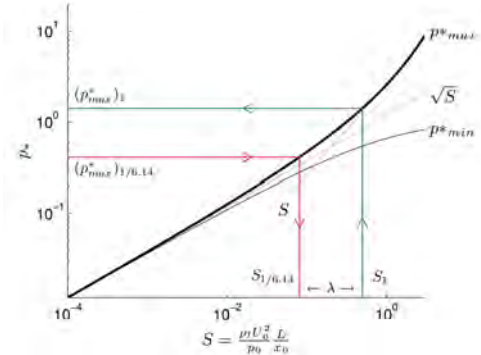
Figure 24. Main parameters of the one-dimensional piston model of Bagnold.

It is assumed that the liquid is incompressible and that the gas is perfect and compressed in a quasi-equilibrium way, so that the pressure is uniform throughout the pocket. The process is moreover considered as adiabatic. Damping of the piston motion is not taken into account. The results for an adiabatic constant of 1.4 – air at standard conditions – are presented in Figure 25. The calculated pressure inside the air pocket is shown as a function of the impact number S . Dimensionless values of the dynamic pressures p_{max}^* and p_{min}^* , and of the time t_r and T are used. These are defined as $p^*=p/p_0$ and $t^*=tU_0/x_0$.

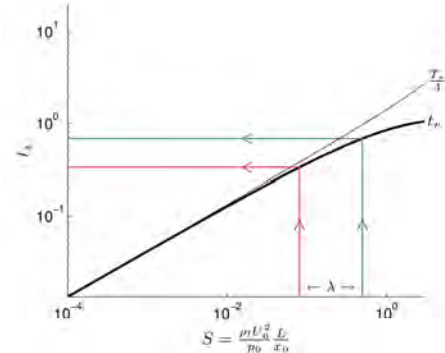
The impact number represents the balance between the pushing liquid and the restoring gas. p_{max}^* increases as S increases. The restoring gas dominates for small values of S , resulting in soft impacts. The pushing liquid dominates for large values of S , resulting in severe impacts. Values of p_{max}^* are given up to 10, i.e. a dynamic pressure of 10 bar for an ullage pressure of 1 bar. The Bagnold model can theoretically go up to much higher pressures but will provide incorrect results since the assumption of a quasi-equilibrium compression is not valid for very severe impacts.

p_{max}^* is proportional to S^α , whereby $\alpha=0.5$ for $S<0.01$ and $\alpha=1$ for $S>1$. Further, T^* is proportional to $4S^{0.5}$ on a large range of S . For small

values of S ($S<0.01$) p_{max}^* equals p_{min}^* and the t_r^* is one fourth of T^* . The time trace is thus sinusoidal when the gas is compressed minimally. As the impact number increases, p_{min}^* becomes smaller than p_{max}^* and t_r^* smaller than one fourth of T^* . The time trace is characterized by a sharp crest and a flat trough when the gas is compressed significantly.



(a) p_{max}^* and p_{min}^* , where $p^* = p/p_0$



(b) t_r^* and T^* , where $t^* = tU_0/x_0$

Figure 25. Dimensionless characteristics of the pressure in the gas pocket for the Bagnold 1D model versus the impact number S .

Bagnold's model can be used to scale the measured pressures in the air pocket when the compressibility of the air is not scaled. The approach is illustrated for test L119 in Figure 25. The first step is to use the curve in Figure 25 (a) to find the S number for the measured p_{max} at large scale. $S_{1/6,14}$ equals 0.08 for the measured $(p_{max})_{1/6,14}$ of 0.4 bar. Next, the impact number at full scale (S_1) is determined. From the definition of the impact number it follows that $S_1 = \lambda S_{1/6,14}$, if the ullage pressure is equal at both scales. The curve is then used again to find the corresponding p_{max} at full scale. $(p_{max})_1$ is 1.4 bar for $S_1=0.50$. With the known values of the S numbers, the frequency of oscillation (T) and the rise time (t_r) can also be found using Figure 25 (b). Table 5 presents the corrected values of p_{max} , t_r and T for L119 and L121.

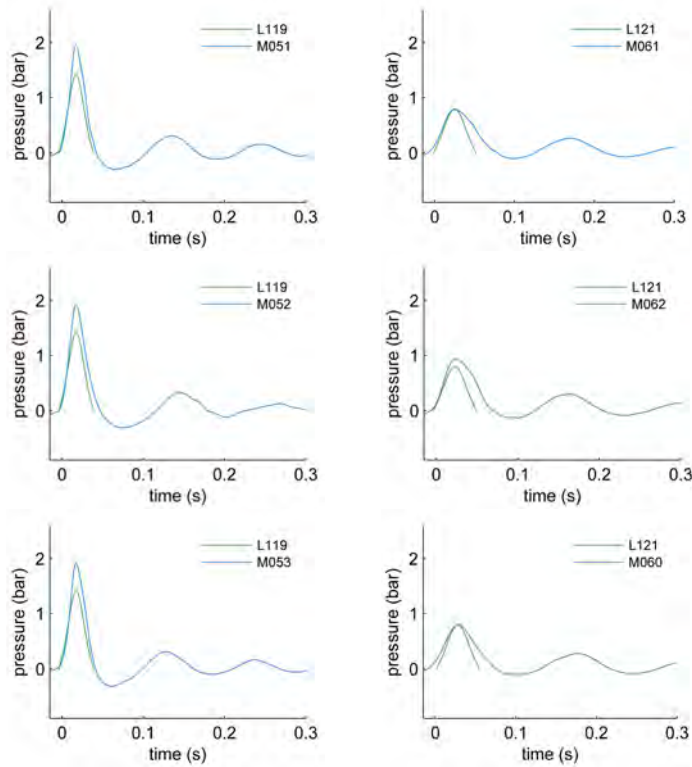
Table 5. Characteristics of the pressure in the air pocket at full scale defined by the Bagnold 1D model ($L119_{Bag}$, $L121_{Bag}$) based on measured pressures at large scale (L119, L121)

	L119	$L119_{Bag}$	$L119_{Bag}/L119$	L121	$L121_{Bag}$	$L121_{Bag}/L121$	
S	(-)	0.08	0.50	6.14	0.04	0.22	6.14
p_{max}	(bar)	0.4	1.4	3.44	0.3	0.8	3.06
t_r	(ms)	5	21	4.13	7	27	3.80
$1/T$	(Hz)	52.7	11.6	1/4.53	45.1	9.3	1/4.85

The pressures in the air pocket scaled according to the Bagnold model are compared to the measured pressures at full scale in Figure 26. The pressures are aligned with the time instant of p_{max} . The pressure

oscillations are only shown for the first half period, because the damping – which is not taken into account in the Bagnold model – increases as time evolves. For test L121, the scaled pressures are very similar to the full scale pressures. For test L119 the scaled pressures are smaller than the pressures at full scale, which is expected because the corresponding full scale tests were less Froude-similar. The air pocket at full scale was smaller, resulting in higher pressures.

The compression of the escaping gas is not taken into account in the Bagnold model, resulting in a sudden start of the pressure. At full scale, the compression of the escaping gas preceded the compression of the entrapped gas, giving a gradual increase of the pressure. This can be seen in the first milliseconds around $t=0$. Furthermore, the damping already affected the first half period causing a longer decay time compared to the rise time. The damping increased during the oscillation of the air pockets because the Kelvin-Helmholtz instabilities develop over time.



(a) Large scale test L119 and full scale tests M51, M52 and M53 (b) Large scale test L121 and full scale tests M61, M62 and M60

Figure 26. Pressures in the air pockets defined by the Bagnold 1D model from large scale (green) and for the measured full scale tests (blue).

The scale factor for p_{max} according to the Bagnold model was not the same for L119 and L121. It was 3.44 for L119 and 3.06 for L121. The scale factor is a function of both the length scale (λ) and the impact number (S). p_{max}^* at model and full scale are proportional to S as follows:

$$(p_{max}^*)_{1/\lambda} \approx S_{1/\lambda}^{\alpha_1/\lambda}, \text{ and } (p_{max}^*)_1 \approx S_1^{\alpha_1}$$

The scale factor is therefore defined as:

$$\frac{(p_{max}^*)_1}{(p_{max}^*)_{1/\lambda}} = \lambda^{\alpha_1} S_{1/\lambda}^{\alpha_1 - \alpha_1/\lambda}$$

If the impact numbers at model and full scale are both smaller than 0.01, $\alpha_1 = \alpha_{1/\lambda} = 0.5$, giving a scale factor for p_{max} of $\lambda^{0.5}$. On the other

hand, if S at model and full scale are both larger than 1 (up to maximum relevant value of the Bagnold model), $\alpha_1 = \alpha_{1/\lambda} = 1$, giving a scale factor for p_{max} of λ . For both L119 and L121, S is in between 0.01 and 1 at model and full scale, resulting in a scale factor between $\lambda^{0.5}$ and λ . Since the entrapped air pocket was smaller and therefore the pressure in the air pocket was larger for L119 than for L121, the S number was higher for test L119. This resulted in a higher scale factor for this test.

4. The development of building jets

The last difference that was observed between the local flows of the large and the full scale tests considers the building jets that were induced by the direct impact of the crest. The development of these building jets along the wall was not similar: jets that ran downward from the crest into the pocket were only observed for the full scale tests. The development of a downward building jet is influenced by the pressure inside the air pocket. It is harder to develop a downward building jet when the air pocket pressure is higher. At large scale, the air pocket pressures were relatively higher and apparently high enough at tests L119 and L121 such that a downward jet was not formed. As a consequence, the liquid that impacted the wall had to change its momentum upwards. This should result in an upward building jet with a relatively higher velocity compared to full scale.

This observation shows that a bias in the compressibility of the gas not only spoils the Froude-scaling of the corresponding ELP ‘compression of entrapped gas’ but also of the ELP ‘building jet’. Therefore, the Froude-scaling of an ELP can be spoiled even if the corresponding phenomenon is appropriately scaled because the ELPs interact. The use of the Bagnold model will therefore only partially correct for the compressibility bias. The experiments could not be used to quantify the influence of the compressibility on the ELP ‘building jet’ as the location of the corrugations was different at both scales. The numerical tools developed in Guilcher et al. (2012) are capable to quantify this difference.

CONCLUSIONS

The impact pressures resulting from breaking waves have been compared deterministically for two different scales in this paper. This comparison is made in order to evaluate by how much the Froude-scaling of the impact pressures is biased by the fact the properties of liquid and gas are not scaled. The comparison was carried out based on the experimental results from Slosheel Joint Industry Project. Unidirectional breaking waves were generated in a flume at scale 1:6 in 2009. These tests were repeated at scale 1:1 in 2010. The piston motions were scaled by maintaining the Froude number. At both scales, the tests were performed with water and air at atmospheric pressure and ambient temperature. The properties of liquid and the gas were therefore equal at both scales.

The wave piston at scale 1:6 was able to mechanically follow the steering signal with a good accuracy, and the resulting waves propagated repeatable through the flume up to the instant before the first contact with the wall. The wave piston at scale 1:1 did not follow the steering signal accurately. A transfer function was used to define steering signals for which the real motion of the piston at scale 1:1 equaled the Froude scaled motion of the piston at scale 1:6. The transfer function significantly improved the accuracy of the piston, resulting in only small differences between the piston motions at both scales.

For the majority of the tests at scale 1:1, the main difference with the tests at scale 1:6 was caused by an uncertainty on the water depth and by the effect of the wind on the propagation of the waves. As a result, many tests at scale 1:1 did not have Froude-similar global flows. Still,

two groups of tests at scale 1:1 had global flows that were Froude-similar to the tests at scale 1:6. In both cases the same type of air pocket impact was generated. One group had very Froude-similar flows so that the differences between the measured pressures at the two scales could be entirely attributed to the fact the properties of the local flow in the vicinity of and during the impacts were not scaled. The other group had flows that were slightly less Froude-similar. Indeed, a smaller air pocket was entrapped at scale 1:1 than at scale 1:6.

The measured pressures at scale 1:6 did not match the measured pressures at scale 1:1 when they are Froude-scaled. The local flows biased the Froude-similarity that was initiated by the global flow. First, the sprays induced by the tangential flow of escaping gas around the tip of the crest were not similar because the surface tension of the liquid was not scaled. The surface tension was therefore relatively higher at scale 1:6, resulting in Kelvin-Helmholtz instabilities with more coherent water films. The effect on the Elementary Loading Processes (Lafeber et al. (2012)) ‘direct impact’ and ‘building jet’ could not be determined by these experiments, because the Kelvin-Helmholtz instabilities make them largely variable at each scale. A large number of tests in combination with a large number of pressure sensors would be required in order to obtain converged statistical pressures. For the same reasons, it was not possible to define the bias of the Froude-scaling by the fact that the compressibility of the liquid was not scaled.

Secondly, the entrapped air was compressed differently at both scales, because the compressibility of the gas was not scaled. The compressibility of the gas was relatively higher at scale 1:6, resulting in relatively higher pressures at scale 1:6 by up to a factor of two. The pressures oscillated moreover with higher frequencies at scale 1:6 than at scale 1:1, by up to a factor of 2.5. These differences had a significant effect on the maximum global forces. The one-dimensional Bagnold model (Bagnold (1939) and Mitsuyasu (1966)) was used to scale the measured pressure in the air pocket at scale 1:6. These scaled pressures were very similar to the measured pressures at scale 1:1 for the first half period of oscillation. The effect of damping which is not taken into account in the Bagnold model – starts to dominate thereafter.

Finally, the development of the building jets were not similar because the compressibility of the gas was not scaled. As the pressure in the air pocket was relatively higher at scale 1:6 than at scale 1:1, it was harder for a downward building jet to develop. The liquid that impacted the wall had to change its momentum upwards, giving an upward building jet with relatively higher velocities at scale 1:6. A gas compressibility bias does thus not only spoil the Froude-scaling of the corresponding ELP ‘compression of entrapped gas’ but also of the ELP ‘building jet’. Therefore, the Froude-scaling of an ELP can be spoiled even if the corresponding phenomenon is appropriately scaled, because the different ELPs interact. Use of Bagnold’s model will therefore only partially correct for the compressibility bias.

Lafeber et al. (2012) found that the bulges of the membrane cargo containment systems also changed the magnitude of the ELPs and the interaction between them. Moreover, Maillard et al. (2009) found that the density between gas and liquid also changed the magnitude and the interaction of the ELPs. The effect of the liquid compressibility and of phase transition on the magnitude and the interaction of the ELPs have not yet been sorted out. Given the above mentioned large variability of the ELP ‘direct impact’ and ‘building jet’, only tests with a deep vacuum in combination with a large number of pressure sensors, or relevant numerical simulations of wave impact with necessarily two compressible fluids and highly refined discretisation in the impact areas as presented in Guilcher et al. (2012) will enable in depth understanding of the effect of liquid compressibility. The effect of phase transition on the ELP ‘compression of entrapped gas’ has been investigated in Ancellin et al. (2012) by an extension of Bagnold’s

piston model based on non-equilibrium thermodynamics (NET). An experimental data set is required to validate this semi-analytical model and to determine the effect on the other ELPs and their interaction.

As the designer of the membrane containment systems for LNG tanks, the main objective of GTT remains the safety of its solutions onboard LNG carriers. GTT relies on empirical scaling factors derived from the feedback at sea, namely from the knowledge that can be drawn from real sloshing incidents on board LNG carriers. Indeed, sloshing model tests have been performed in order to mimic accurately real voyages that led to a certain amount of slightly damaged NO96 boxes or permanently deformed MarkIII corrugation within tanks of LNG carriers. The empirical scaling factors are fitted in order the probability of failure derived from GTT’s sloshing assessment methodology matches the real ones.

At the same time a research strategy is being developed in order to derive scaling factors more directly: a complete understanding of the scaling biases will enable improving the experimental modeling represented by sloshing model tests and defining the best way to scale the measured pressures despite the remaining biases.

ACKNOWLEDGEMENTS

The authors would like to acknowledge the support provided by the SlosheL consortium members that have made the SlosheL project possible: American Bureau of Shipping, Bureau Veritas, Ecole Centrale Marseille, Chevron, ClassNK, Det Norske Veritas, GDF SUEZ, GTT, Lloyd’s Register, MARIN, Total and Shell.

The views expressed in the paper are those of the authors and do not commit the other SlosheL consortium members.

REFERENCES

- Ancellin, M., Brosset, L. and Ghidaglia, J.-M., (2012). *Influence of phase transition on sloshing impact pressures described by a generalized Bagnold’s model*, Proceedings of 22nd International Offshore and Polar Engineering Conference, June 17-22, Rodos, Greece.
- Bagnold, R., (1939). *Interim report on wave-pressure research*, J. Inst Civil Eng. **12**: 201-226.
- Bogaert, H., Léonard, S., Brosset, L. and Kaminski, M., (2010). *Sloshing and scaling: results from SlosheL project*, Proceedings of 20th International Offshore and Polar Engineering Conference, June 20-26, Beijing, China.
- Braeunig, J.-P., Brosset, L., Dias, F. and Ghidaglia, J.-M., (2009). *Phenomenological study of liquid impacts through 2D compressible two-fluid numerical simulations*, Proceedings of 19th International Offshore and Polar Engineering Conference, June 21-26, Osaka, Japan.
- Brosset, L., Lafeber, W., Bogaert, H., Marhem, M., Carden, E.P. and Maguire, J.R., (2011). *A MarkIII panel subjected to a Flip-trough impact: Results from the SlosheL project*, Proceedings of 21st International Offshore and Polar Engineering Conference, June 19-24, Hawaii, USA.
- Brosset, L., Mravak, Z., Kaminski, M., Collins, S. and Finnigan, T., (2009). *Overview of SlosheL project*, Proceedings of 19th International Offshore and Polar Engineering Conference, June 21-26, Osaka, Japan.
- Gervaise, E., de Sèze, P.E. and Maillard, S. (2009). *Reliability-based methodology for sloshing assessment of membrane LNG vessels*, Proceedings of 19th International Offshore and Polar Engineering Conference, June 21-26, Osaka, Japan.

Guilcher, P.M., Brosset, L., Couty N. and Le Touzé, D. (2012). *Simulations of breaking wave impacts on a rigid wall at two different scales with a two phase fluid compressible SPH model*, Proceedings of 22nd International Offshore and Polar Engineering Conference, June 17-22, Rodos, Greece.

Hinze, J.O., (1955), *Fundamentals of the hydrodynamic mechanism of splitting in dispersion processes*. AICHE Journal 1(3), 289-295.

Kaminski, M.L. and Bogaert, H. (2010). *Full-Scale Sloshing Impact Tests Part II*, Proceedings of 20th International Offshore and Polar Engineering Conference, June 20-26, Beijing, China.

Kimmoun, O., Ratouis, A., Brosset, L., (2010), *Sloshing and scaling: experimental study in a wave canal at two different scales*, Proceedings of 20th International Offshore and Polar Engineering Conference, June 20-26, Beijing, China.

Lafeber, W., Brosset, L., Bogaert, H., (2012). *Elementary Loading Processes (ELP) involved in breaking wave impacts: findings from the SlosheI project*, Proceedings of 22nd International Offshore and Polar Engineering Conference, June 17-22, Rodos, Greece.

Maillard, S., Brosset, L., (2009), *Influence of density ratio between liquid and gas on sloshing model tests results*, Proceedings of 19th International Offshore and Polar Engineering Conference, June 21-26, Osaka, Japan.

Mitsuyasu, H. (1966), *Shock pressure of breaking wave*, Proc. of 10th Int. Conf. Coastal Eng.

Copyright ©2012 The International Society of Offshore and Polar Engineers (ISOPE). All rights reserved.